JGR Oceans

RESEARCH ARTICLE
10.1029/2020JC016197

The Atlantic Water Boundary Current in the Chukchi Borderland and Southern Canada Basin

Jianqiang Li[1], Robert S. Pickart[2], Peigen Lin[2], Frank Bahr[2], Kevin R. Arrigo[3], Laurie Juranek[4], and Xiao-Yi Yang[1]

[1]State Key Laboratory of Marine Environmental Science, and College of Ocean and Earth Sciences, Xiamen University, Xiamen, China, [2]Woods Hole Oceanographic Institution, Woods Hole, MA, USA, [3]Department of Earth System Science, Stanford University, Stanford, CA, USA, [4]College of Earth, Ocean and Atmospheric Sciences, Oregon State University, Corvallis, OR, USA

Key Points:
- The Atlantic Water boundary current has two branches in the southern Canada Basin, flowing beneath and counter to the Beaufort Gyre
- The two branches emerge from the Chukchi Borderland due to a series of bifurcations of the single branch that enters the Borderland
- The propagation of warm temperature anomalies through the region is consistent with the deduced circulation scheme

Correspondence to:
R. S. Pickart,
rpickart@whoi.edu

Citation:
Li, J., Pickart, R. S., Lin, P., Bahr, F., Arrigo, K. R., & Juranek, L., et al. (2020). The Atlantic water boundary current in the Chukchi Borderland and southern Canada Basin. *Journal of Geophysical Research: Oceans*, *125*, e2020JC016197. https://doi.org/10.1029/2020JC016197

Received 1 MAR 2020
Accepted 22 JUL 2020
Accepted article online 27 JUL 2020

Abstract Synoptic shipboard measurements, together with historical hydrographic data and satellite data, are used to elucidate the detailed structure of the Atlantic Water (AW) boundary current system in the southern Canada Basin and its connection to the upstream source of AW in the Chukchi Borderland. Nine high-resolution occupations of a transect extending from the Beaufort shelf to the deep basin near 152°W, taken between 2003 and 2018, reveal that there are two branches of the AW boundary current that flow beneath and counter to the Beaufort Gyre. Each branch corresponds to a warm temperature core and transports comparable amounts of Fram Strait Branch Water between roughly 200–700 m depth, although they are characterized by a different temperature/salinity (T/S) structure. The mean volume flux of the combined branches is 0.87 ± 0.13 Sv. Using the historical hydrographic data, the two branches are tracked upstream by their temperature cores and T/S signatures. This sheds new light on how the AW negotiates the Chukchi Borderland and why two branches emerge from this region. Lastly, the propagation of warm temperature anomalies through the region is quantified and shown to be consistent with the deduced circulation scheme.

Plain Language Summary Warm water flows into the Arctic Ocean from the North Atlantic and circulates counterclockwise through the different subbasins of the Arctic. The water is cooled, freshened, and densified as part of the global overturning circulation. The warm water also spreads into the interior Arctic with the potential to melt sea ice. Presently, very little is known about the Atlantic Water (AW) circulation in the Canada Basin, far from the source of the water. In this study, we analyze nine repeat shipboard transects extending from the Beaufort Sea shelf to the deep basin, taken between 2003 and 2018. The transects reveal that there are two branches of the AW boundary current, each characterized by a warm temperature core. The branches transport roughly equal amounts of water. Using an extensive historical database, we demonstrate that the two branches emerge from a region of complex topography known as the Chukchi Borderland. A single AW current entering the Borderland undergoes a series of divisions and merges, which ultimately forms two branches that are further distinguishable by their temperature and salinity structure. Finally, we document the propagation of warm temperature pulses through the region, which is consistent with the deduced circulation scheme.

1. Introduction

As far back as the early twentieth century it was recognized that the warm, intermediate layer of the Arctic Ocean originated from the North Atlantic Ocean (Nansen, 1902). Since that time, studies have investigated the intricate pathways, mixing, and impact of this water throughout the Arctic basin. The transformation of the Atlantic Water (AW) during this northern excursion contributes to the global meridional overturning circulation, and the spreading of the warm water into the basin interiors fundamentally dictates the thermohaline structure of the Arctic water column (Rudels, 2012). In the Eurasian Basin the upward heat flux of AW can reach the surface and contribute to sea ice melt (Polyakov et al., 2010), and upwelling of AW along the margins of the Canada Basin can cause ice melt there (Ladd et al., 2016). While we have gained an increased understanding of the importance of AW through these studies, our view remains incomplete. This is particularly true in the Canadian sector of the Arctic Ocean, where basic questions remain regarding the path, structure, and transport of AW.

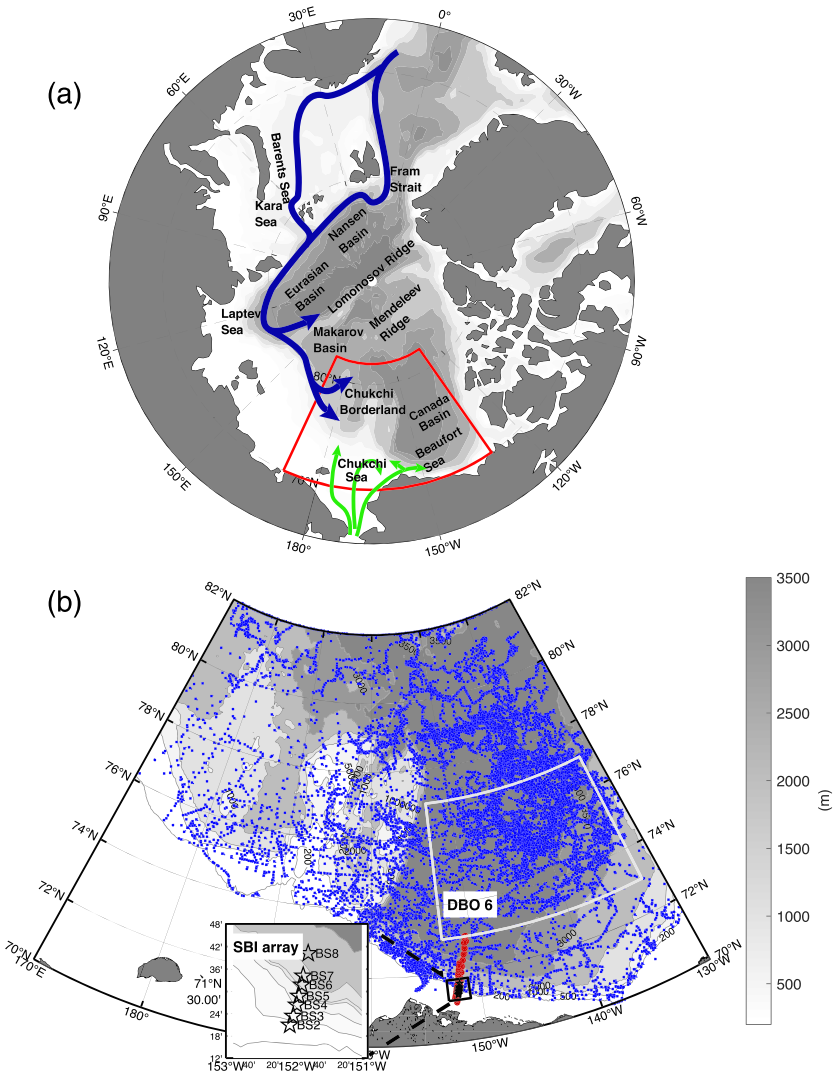

Figure 1. (a) Schematic circulation of the Atlantic Water (blue arrows) and Pacific Water (green arrows) and relevant place names. The shaded bathymetry is from IBCAO v3. The area denoted by red lines is enlarged in (b), which is the domain considered in the present study. (b) Occupations of the DBO6 transect (red circles) and lateral coverage of the UDASH hydrographic data (blue dots). The region delimited by the white lines is the area over which the wind stress curl was computed. The area showing the SBI moorings (black stars) is enlarged.

AW enters the Arctic via Fram Strait and the Barents Sea. The former is referred to as Fram Strait Branch Water (FSBW), which is warm and salty and occupies the depth range 150–600 m in the Nansen Basin (Pérez-Hernández et al., 2019), while the latter is cooler and fresher and is known as Barents Sea Branch Water (BSBW), centered at roughly 700 m (McLaughlin et al., 1996; Schauer et al., 2002). Shipboard observations and moored measurements indicate that the boundary current transporting the AW is strongly tied to topography and flows cyclonically along the margins of the Arctic basins (Aksenov et al., 2011; Rudels et al., 1994; see Figure 1). Three different branches of AW emerge from Fram Strait (Cokelet et al., 2008; Koenig et al., 2017; Kolås & Fer, 2018; Meyer et al., 2017) which are believed to combine into a single boundary current along the continental slope north of Svalbard. Based on data from a year-long mooring array, the transport of AW at this location is 2.08 ± 0.24 Sv (Pérez-Hernández et al., 2019).

Farther to the east, the outflow of BSBW from St. Anna Trough combines with, and partially subducts under, the FSBW (Schauer et al., 2002). Using 2 years of mooring data from the Laptev Sea continental slope, Pnyushkov et al. (2018) computed a mean AW volume transport of 3.1 ± 0.1 Sv. As the current continues

eastward it then encounters the Lomonosov Ridge and bifurcates, with some of the flow progressing along the ridge and some of it continuing along the continental slope into the Canadian Basin. Woodgate et al. (2001) estimated that ~3 Sv continues eastward along the continental slope into the Canadian Basin.

Beyond this point the circulation pathways are less clear, although the AW signal has been traced by its temperature maximum (Swift et al., 1997). An additional part of the flow is believed to be channeled into the interior along the Alpha-Mendeleev Ridge (Rudels et al., 1994), and different branches of the FSBW are thought to progress through the complex topography of the Chukchi Borderland. Shimada et al. (2004) discuss a northern pathway of AW around the outside of the Borderland—that is, along the edge of the Chukchi Rise and Northwind Ridge (see also McLaughlin et al., 2009; Woodgate et al., 2007)—and a southern pathway along the Chukchi Sea continental slope. Shimada et al. (2004) argue that AW progresses eastward toward the Canada Basin via both routes, with the southern route taking less time. In addition, tracer measurements suggest that a portion of the AW is diverted from the outer part of the Chukchi Borderland into the deep Canada Basin (Smith et al., 1999).

Farther to the east, in the vicinity of the Beaufort Sea, very little is known about the flow of AW, although some of it is believed to participate in the anticyclonic Beaufort Gyre (McLaughlin et al., 2009; Newton & Coachman, 1974). Using a 2 year mooring data set on the Beaufort continental slope that extended out to the 1,400 m isobath, Nikolopoulos et al. (2009) computed a mean AW transport of 0.048 $\pm$ 0.026 Sv, but the array sampled only the inshore edge of the current. The eastward flow was found to be highly variable. Using the same data set with a simple numerical model, Pickart et al. (2011) deduced that the AW transport is periodically enhanced at this location following wind-driven upwelling events (see also Lin et al., 2019). Until now, however, there have been no direct velocity measurements of the AW boundary current in the region offshore of the array.

The seasonal variation of AW hydrographic properties varies around the perimeter of the Arctic Ocean, although east of the Lomonosov Ridge, in the Makarov and Canada Basins, no significant seasonality has been found (Lique & Steele, 2012). On decadal time scales, the temperature of the AW layer oscillates on a period of 50–80 years (Polyakov et al., 2004). It was shown by Polyakov et al. (2004) that these changes are in concert with similar variations occurring in the Nordic Seas, implying that the Arctic variability is driven by changes in the AW inflow through Fram Strait (see also Polyakov et al., 2005). Superposed on these decadal oscillations are interannual events, or pulses, where significantly warmer water flows through Fram Strait and subsequently progresses cyclonically around the Arctic Ocean in the boundary current (e.g., Dmitrenko et al., 2008; Polyakov et al., 2005, 2010).

In this paper we investigate the flow of AW in the Canada Basin, far from the two source regions of the warm water, where direct measurements of the flow are rare. We use a set of nine shipboard sections occupied between 2003 and 2018 along a transect spanning from the outer Beaufort shelf into the Canada Basin. The sections included direct measurements of the velocity along with the hydrography. This offers a first quantitative view of the AW boundary current structure and transport at this location, revealing that there are two branches of the current: one at the base of the continental slope and one farther offshore in the Canada Basin. We then use a historical database of hydrographic measurements to investigate why there are two branches. In particular, we map the temperature cores of the AW from the Chukchi Borderland to our transect, and also make use of characteristic temperature/salinity (T/S) signatures to shed light on the nature of the flow. Finally, we address the interannual variations of the AW and how the warm pulses propagate through the region.

2. Data and Methods

2.1. Shipboard Data

Between 2003 and 2018, a hydrographic section extending from the shelf to the basin in the Alaskan Beaufort Sea near 152°W was repeated nine times on the USCGC *Healy*, R/V *Nathan B. Palmer*, and R/V *Sikuliaq* (Figure 1b and Table 1). Recently, the transect has become part of the Distributed Biological Observatory (DBO) program (Moore et al., 2018) and is referred to as the DBO6 line. Two important aspects of the occupations considered here are that (1) they extend well into the basin with a spatial resolution that adequately resolves the components of the boundary current system, typically 5 km in the vicinity of the

Table 1
Occupations of the DBO6 Transects Used in the Study

Cruise	Ship	Year	Date	Shipboard ADCP	ADCP acquisition code
NBP03	R/V *N.B. Palmer*	2003	12–14 Aug	NB150	DAS 2.48
HLY1003	USCGC *Healy*	2010	13–15 Sep	OS150NB	UHDAS
HLY1101	USCGC *Healy*	2011	20–22 Jul	OS150NB	UHDAS
HLY1103	USCGC *Healy*	2011	10–11 Oct	OS150NB	UHDAS
HLY1203	USCGC *Healy*	2012	12–14 Oct	OS150NB	UHDAS
HLY1303	USCGC *Healy*	2013	16–18 Oct	OS150NB	UHDAS
HLY1402	USCGC *Healy*	2014	16–18 Jul	OS150NB	UHDAS
SKQ16	R/V *Sikuliaq*	2016	8–9 Sep	OS150NB	UHDAS
HLY1803	USCGC *Healy*	2018	30 Oct to 1 Nov	OS150NB	UHDAS

shelfbreak and upper slope, and 20 km in the basin (by contrast, a typical occupation of the DBO6 line extends only to the midcontinental slope); and (2) direct velocity measurements were taken during each of the occupations.

The seasonal timing of the transects ranges from mid-July to late-October (Table 1). The stations were typically taken to 800 m depth, or to the bottom where the topography is shallower than this. The exception is the 2003 *Palmer* cruise in which the stations were only taken to 500 m depth. The entire transect usually took ~2 days to complete. In the analysis we truncated the section 185 km seaward of the shelfbreak because only three occupations went beyond that. Furthermore, three of the occupations sampled Pacific Water eddies, which are found in the southern Canada Basin (e.g., Pickart et al., 2005; Spall et al., 2008). These anomalous signatures were removed from the transects in question to avoid aliasing the mean sections.

Each of the cruises used a Sea-Bird 911p conductivity-temperature-depth (CTD) instrument attached to a rosette with 12-L or 30-L Niskin bottles for water collection. In each case the temperature and conductivity sensors were calibrated at Sea-Bird prior to and after the field season. In addition, the conductivity sensors were usually subject to an in situ calibration using salinity samples from the Niskin bottles. Accuracies are estimated to be 0.001°C for temperature and 0.008 for salinity.

Velocity measurements were obtained on each cruise from a hull-mounted acoustic Doppler current profiler (ADCP), see Table 1. The *Healy* and *Sikuliaq* data sets were collected with 150 kHz Teledyne RD Instrument Ocean Surveyors, while the *Palmer* data set was collected with an older-style RDI NB150 instrument. High-quality differential GPS and/or inertial navigation heading devices (e.g., Ashtech, Seapath) were available for all cruises. The University of Hawaii's CODAS processing routines (http://currents.soest.hawaii.edu) were employed for all data sets. As is common for high-latitude cruises, substantial manual editing was required to address ice interference. Barotropic tides were estimated using the Oregon State University tidal model and removed from the final data sets (http://volkov.oce.orst.edu/tides; Padman & Erofeeva, 2004).

We constructed vertical sections of potential temperature, salinity, and potential density. This was done using Laplacian-Spline interpolation with a horizontal grid spacing of 5 km and vertical grid spacing of 5 m. The bottom topography along the DBO6 line was obtained from *Healy's* echo sounder, corrected for sound speed using the CTD data. Absolute geostrophic velocities were computed using the gridded data, referenced using the gridded vessel-mounted ADCP data. In particular, the relative geostrophic profile for each set of neighboring grid points was referenced using the average cross-track velocity for the grid points, where the matching was done over the common depth range of the CTD and vessel-mounted ADCP. Vertical sections of absolute geostrophic velocity were constructed in the same fashion as for the hydrographic variables.

2.2. Historical Hydrographic Data

For part of the analysis we use historical hydrographic data from the Unified Database for Arctic and Subarctic Hydrography (UDASH), which are found at this site (https://doi.pangaea.de/10.1594/PANGAEA.872931). This is a collection of vertical profiles of temperature and salinity for the region north

of 65°N, for the period 1980–2015. The data sources are CTDs, ice-tethered profilers, and Argo floats (see Behrendt et al., 2018, for details). The data coverage in our region of interest is shown in Figure 1b.

2.3. Satellite Sea Surface Data

We use the altimetry-derived sea surface height data set described in Armitage et al. (2016), which has monthly resolution from 2003–2014. In ice-covered regions the absolute dynamic topography is estimated from openings in the pack-ice, which is combined with the conventional open ocean altimetry product to produce the monthly fields. The sea surface height is relative to the GOCO03s geoid (Mayer-Gürr et al., 2012). The spatial resolution of the product is 0.25° and 0.75° in the meridional and zonal directions, respectively, and the data coverage extends to 81.5°N.

2.4. Mooring Data

A mooring array was deployed over the Alaskan Beaufort shelfbreak and slope near 152°W from 2002 to 2004, as part of the Western Arctic Shelf-Basin interactions (SBI) program (Figure 1b). Seven moorings (BS2–BS8) were located from onshore to offshore. Hydrographic measurements were obtained using a moored CTD profiler, which provided vertical traces of temperature and salinity multiple times per day extending from near the sea floor to approximately 40 m beneath the surface. Velocity measurements were obtained every hour on moorings BS2–BS6 using upward facing, bottom-mounted ADCPs, and every 12 hr on moorings BS7–BS8 using acoustic current meters. The reader is referred to Spall et al. (2008) and Nikolopoulos et al. (2009) for a detailed description of the SBI hydrographic and velocity mooring measurements, respectively, used in the present study.

2.5. Wind Information

We use wind data from the meteorological station in Utqiaġvik, AK (formerly known as Barrow, AK). These were obtained from the National Climate Data Center of the National Oceanic and Atmosphere Administration (http://www.ncdc.noaa.gov/). The data were quality controlled as described in Pickart et al. (2013) and have a temporal resolution of 1 hr. We used the alongcoast component, which is 105°T. Previous studies have shown that the winds at Utqiaġvik are representative of the region near the DBO6 transect (e.g., Nikolopoulos et al., 2009; Pickart et al., 2009). To characterize the atmospheric forcing over a broader area we use the 10 m winds from the ERA5 reanalysis product. ERA5 is the fifth-generation European Centre for Medium-Range Weather Forecast (ECMWF) atmospheric global reanalysis, which has a 0.25° horizontal spacing and 3-hourly temporal resolution. The data were obtained from this site (https://www.ecmwf.int/en/forecasts/datasets/reanalysis-datasets/era5).

3. Repeat Sections of the Atlantic Water Boundary Current

3.1. Mean State

3.1.1. Context

Numerous previous studies have investigated the Pacific water boundary current in the Alaskan Beaufort Sea using data collected near the location of the DBO6 transect (e.g., Lin et al., 2016; Nikolopoulos et al., 2009; Pickart et al., 2011). The current is centered at the shelfbreak—known as the Beaufort shelfbreak jet—and in the mean it flows eastward with a transport that varies interannually between 0.02 and 0.12 Sv (Brugler et al., 2014). Much of our knowledge of the Beaufort shelfbreak jet (including documentation of its existence) comes from the SBI mooring array deployed across the current from 2002–2004 (described in section 2.4). The array extended to the 1,400 m isobath, which was far enough offshore to capture some eastward flow of AW. The mooring positions are shown in Figure 1b, where mooring BS3 corresponds to the center of the shelfbreak jet.

The two-year mean potential temperature and velocity fields from the mooring array provide context for the present study. In the mean, the 27.06 kg m^{-3} isopycnal represents the interface between the Pacific water and the AW (Nikolopoulos et al., 2009). The cold Pacific winter water layer is evident by a minimum in temperature centered at 120 m depth (Figure 2a). The reason why the temperatures are colder offshore is that wind-driven upwelling regularly brings AW to the vicinity of the shelfbreak, which, in the mean, moderates the temperature there. Above the winter water resides the Pacific summer water layer, which is warmest near the shelfbreak. Below the winter water is the AW, with a temperature maximum associated with the FSBW – the focus of this study.

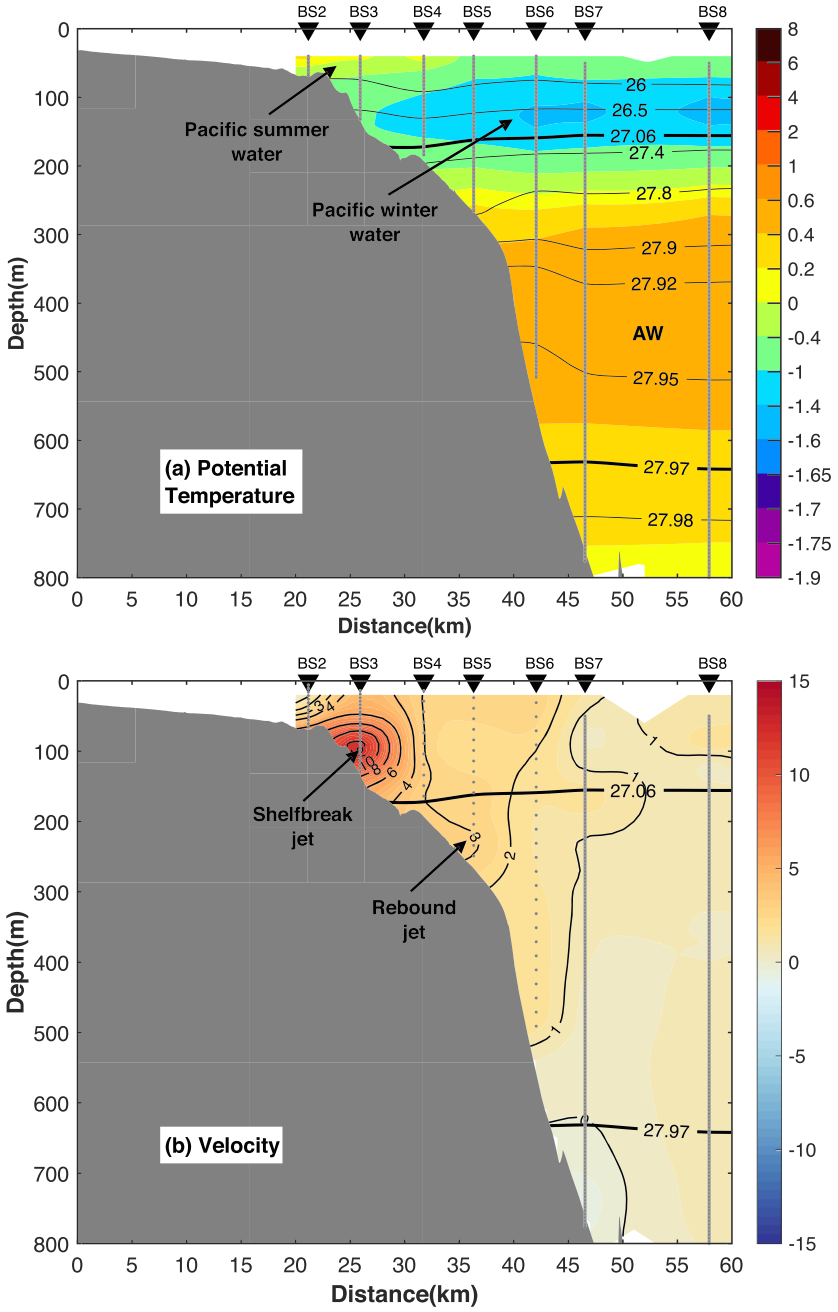

Figure 2. Two-year mean sections from the SBI mooring array. (a) Potential temperature (color, °C) overlain by potential density (contours, kg m^{-3}). The gray lines show the data coverage, and the symbols along the top denote the moorings. The 27.06 density contour is highlighted, which marks the boundary between the Pacific Water and AW. (b) Alongstream velocity (color and contours, cm s^{-1}), where positive is directed toward 125°T (the direction of the mean flow). The gray dots/lines show the data coverage.

The mean velocity field from the mooring array is dominated by the presence of the shelfbreak jet which is bottom-intensified and advects Pacific water to the east (Figure 2b). Seaward of this there is enhanced flow of AW adjacent to the upper continental slope, referred to as the "rebound jet" by Pickart et al. (2011), which instantaneously can reach speeds exceeding 50 cm s^{-1}. Pickart et al. (2011) demonstrated that this is an intermittent wind-driven feature. In particular, at the end of an upwelling event, a deep jet of AW is spun up for several days due to the shelf wave adjustment resulting from the cessation of the easterly winds.

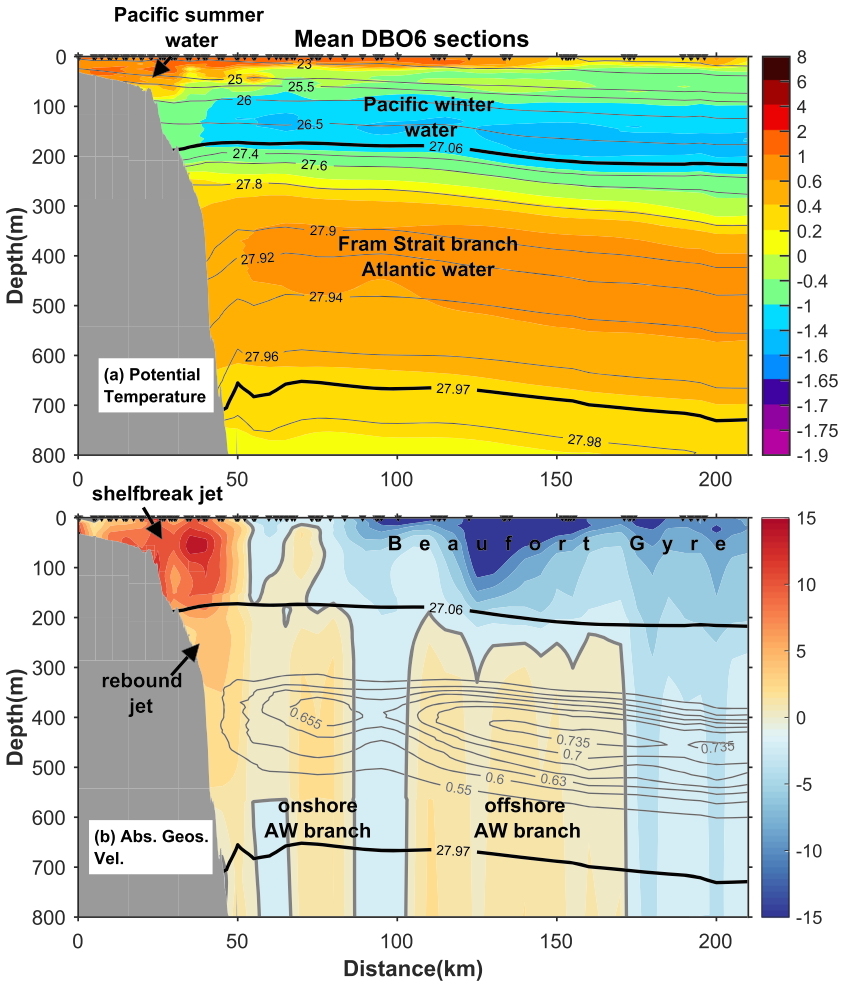

Figure 3. Mean sections of the nine DBO6 occupations. (a) Potential temperature (color, °C) overlain by potential density (contours, kg m^{-3}). The 27.07 and 27.97 isopycnals are highlighted, corresponding to the upper and lower bounds of the FSBW. The station locations are marked along the top of the plot (inverted triangles). The different water masses are labeled. (b) Absolute geostrophic velocity (color, cm s^{-1}) normal to the transect. Positive velocities are eastward. The light gray contours are temperature (°C) within the FSBW layer. The different components of the circulation are labeled.

Because upwelling is so prevalent over the course of the year, there is a signature of the rebound jet in the mean, although, as noted above, its average transport is quite small (less than 0.05 Sv).

3.1.2. Hydrography

The SBI mooring array extended ~40 km seaward of the shelfbreak and hence captured only the edge of the AW layer. The DBO6 shipboard transects, on the other hand, generally extended well into the basin, roughly 175 km beyond the shelfbreak (Figure 1b). The mean vertical sections of the nine occupations are shown in Figure 3. The same layering of water masses is present as was seen from the SBI array (cf. Figures 2a and 3a): Pacific summer water with an enhanced signal near the shelfbreak; Pacific winter water beneath this corresponding to a temperature minimum; and AW with a temperature maximum associated with the FSBW centered near 400–500 m. Both the Pacific winter water and AW temperature signals are stronger offshore. The dampening of these signals near the upper slope is likely due to enhanced mixing during the upwelling events as well as during downwelling events that bring cold water to depth.

As noted above, the upper boundary of the FSBW is taken to be the 27.06 kg m^{-3} isopycnal, which corresponds to the maximum in stratification at the base of the Pacific winter water layer (see Nikolopoulos et al., 2009). It is less clear what to use for the lower boundary, that is, the interface between the FSBW

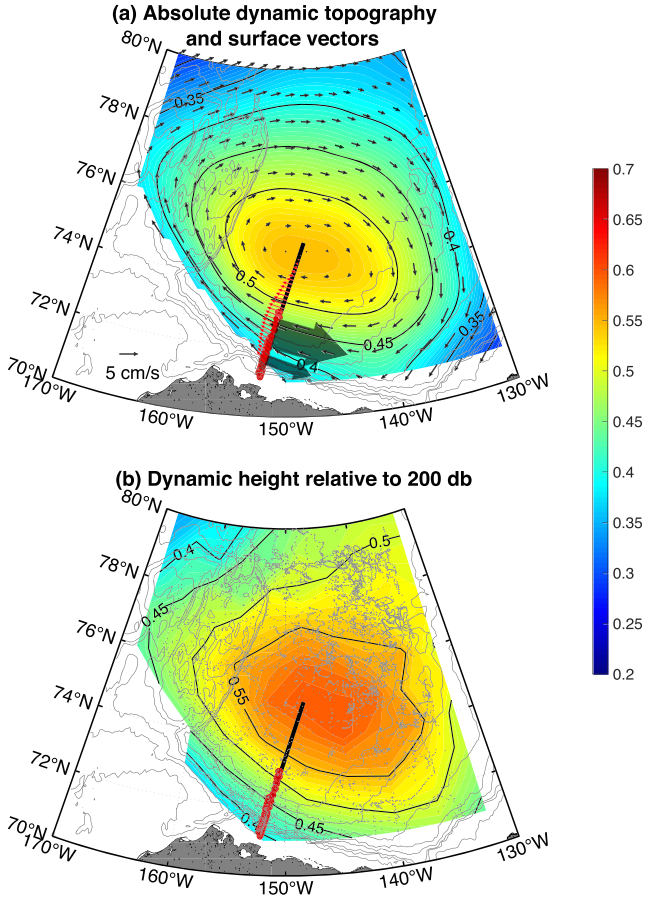

Figure 4. (a) Mean absolute dynamic topography of the sea surface (color and contours; m) and corresponding surface geostrophic velocity (thin black vectors, subsampled every fourth point). The black line is the section along which the Beaufort Gyre transport is calculated using the historical hydrographic data, and the red vectors were used for the calculation. The red circles are the DBO6 station positions. The semitransparent black arrows show the mean location of the two AW branches investigated in this study (these are not drawn to scale, but are accurate in their cross-stream location). The light gray contours are the bathymetry. (b) Mean dynamic height of the sea surface relative to 200 db using the UDASH data (color and contours, m). The small gray dots denote the UDASH data points.

and BSBW. Both Woodgate et al. (2007) and Dosser and Timmermans (2018) indicate that the core of the BSBW is near 28 kg m^{-3}, and that its upper boundary is near 700 m. Here we choose the 27.97 kg m^{-3} isopycnal as the interface, which is ~700 m (Figure 3a). This is also close to the isopycnal (27.98 kg m^{-3}) that McLaughlin et al. (2009) used. We note that the results presented below are not sensitive to the precise choice of the interface. The two bounding isopycnals of the FSBW are highlighted in Figures 2 and 3.

3.1.3. Beaufort Gyre

The mean absolute geostrophic velocity section (Figure 3b) shows the presence of both the shelfbreak jet advecting Pacific water, and the rebound jet advecting AW. Farther offshore there is surface-intensified westward flow associated with downward tilting isopycnals progressing offshore into the basin. This is the southern portion of the Beaufort Gyre, the signature of which is present in all nine transects. Using the mean section of Figure 3b, the transport of this westward flow is 1.99 Sv, where the integration is taken from a distance of 80 km to the end of the section, and from the surface to the 27.06 isopycnal (Figure 3b).

To our knowledge there are no other published observational estimates of the Beaufort Gyre volume transport. However, the transport can be estimated using the satellite absolute dynamic topography data (ADT) together with the water column data from UDASH. To be consistent with the time period of the DBO6 occupations (Table 1), for this calculation we used the ADT and UDASH data during July to November. The mean ADT over this time period in the Canada Basin shows the doming of the sea surface associated with the Beaufort Gyre (Figure 4a). The corresponding surface geostrophic velocity vectors reveal the anticyclonic circulation of the gyre, with a maximum speed of roughly 5 cm s^{-1}. By way of comparison, the mean dynamic height of the sea surface relative to 200 db from the UDASH data (Figure 4b) shows a similar doming of the gyre (where we have applied Laplacian smoothing to reduce the small-scale noise).

We constructed a vertical section of thermal wind shear relative to the surface, using the UDASH data, by extracting all of the profiles within 25 km of the black line in Figure 4, then interpolating the data onto a regular grid. The relative geostrophic velocities were then made absolute by referencing them to the ADT-derived surface geostrophic velocities—in particular, the cross-track component of the red vectors in Figure 4a. Since the satellite product has relatively larger errors near the southern boundary of the Canada Basin, we excluded the part of the section near the Beaufort continental slope. Integrating to a depth of 200 m (or equivalently to the 27.06 kg m^{-3} isopycnal), the resulting Beaufort Gyre transport is 1.43 Sv, compared to the value of 1.99 Sv calculated using the mean shipboard section of Figure 3b. In light of the differences between the two approaches, that is, a space-time composite over decades referenced using satellite data, versus an average of synoptic crossings referenced using shipboard velocity data, the agreement is encouraging. It should be noted that, according to the surface geostrophic velocity vectors of Figure 4a, the mean DBO6 section (the red circles in Figure 4a) did not capture the complete gyre, although the flow near the gyre center is very weak.

3.1.4. AW Velocity

In the mean DBO6 velocity section of Figure 3b, beneath the Beaufort Gyre in the AW layer offshore of the rebound jet, there are two deep-reaching, eastward flowing velocity cores. Notably, each core corresponds to an extremum in temperature of the FSBW (the temperature signals are weak, but significant; Figure 3b). We

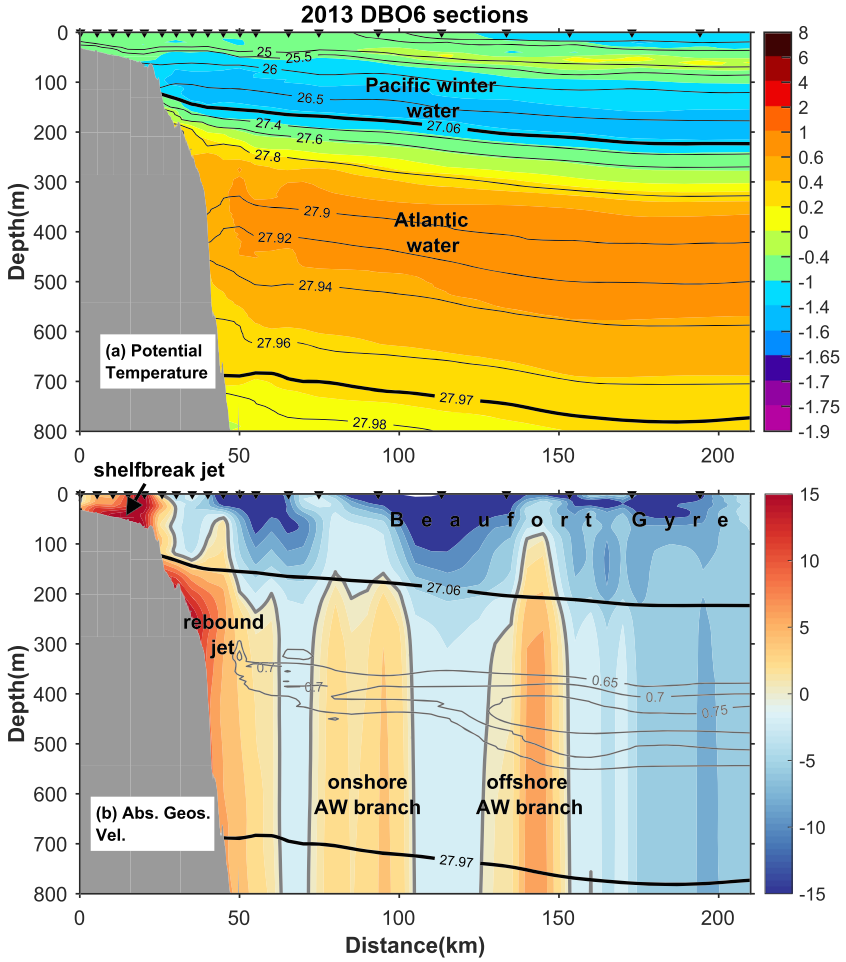

Figure 5. Same as Figure 3 except for the 2013 occupation of the DBO6 line.

conclude from this that there are two branches of the AW current in the Canada Basin, which we will refer to as the onshore and offshore branch, respectively. Although the branches extend into the BSBW, our data do not extend deep enough to address this component of the AW; from here on, all discussion of the branches refers to the FSBW.

The mean speed of the onshore branch is 1.2 ± 1.0 cm s^{-1}, while that of the offshore branch is 0.8 ± 0.3 cm s^{-1} (the uncertainty is the standard error). These values are not that different from the measured speed of 2 cm s^{-1} for the AW entering the Canadian Basin east of the Lomonosov Ridge (Woodgate et al., 2001). We note that both branches were present in all nine occupations, but the offshore branch was not completely bracketed in the July 2011 occupation, and the onshore branch in that occupation was influenced by a deep-reaching Pacific Water eddy. Hence, we were unable to calculate the transport of either AW branch for that transect. The same is true for the 2003 section since the stations were not taken deep enough to span the entire FSBW layer (These two sections were used for all other calculations in the analysis, aside from the AW transport.). The lateral positions of the branches varied somewhat from realization to realization, leading to a weaker mean signal. Instantaneously, the signature of the branches can be stronger. For example, Figure 5 shows the October 2013 occupation in which the onshore branch is ~4 cm s^{-1} and the offshore branch is ~7 cm s^{-1}. The rebound jet is significantly stronger in this occupation as well. Overall, the onshore branch is found between the 1,000–1,500 m isobaths, and the offshore branch between the 2,500–3,000 m isobaths. The location of the two branches in relation to the long-term mean Beaufort Gyre is shown by the two arrows in Figure 4a (these are not drawn to scale, but are accurate in their cross-stream

Table 2
Volume Transports of the AW Branches

Cruise	Year	Onshore branch (Sv)	Offshore branch (Sv)	Total (Sv)
NBP03	2003	—	—	—
HLY1003	2010	0.16	0.62	0.78
HLY1101	2011	—	—	—
HLY1103	2011	0.54	0.24	0.78
HLY1203	2012	0.62	0.73	1.35
HLY1303	2013	0.33	0.38	0.71
HLY1402	2014	0.62	0.56	1.18
SKQ16	2016	0.26	0.71	0.97
HLY1803	2018	0.23	0.03	0.26
Mean value		0.40±0.07	0.47±0.10	0.87±0.13

location). This indicates that the offshore branch is beneath the strong flow of the gyre, consistent with the vertical section of Figure 3b.

We computed the volume transport of each AW branch for the seven occupations where this was possible, integrating from the 27.06 kg m^{-3} isopycnal to the 27.97 kg m^{-3} isopycnal (i.e., the FSBW). These are shown in Table 2. The mean transport of the inner branch is 0.40 ± 0.07 Sv, and that of the outer branch is 0.47 ± 0.10 Sv, totaling 0.87 ± 0.13 Sv. The range of total transports was 0.26 Sv (November 2018) to 1.18 Sv (July 2014). As noted in section 1, Woodgate et al. (2001) estimated a transport of 3.1 Sv for the AW entering the Canadian Basin along the continental slope. However, this included the BSBW and their calculation used only a single mooring, with assumptions about the width of the flow. On the other hand, our data nicely resolve the cross-sectional structure of flow, although we have a relatively small number of snapshots.

3.2. Variability

As seen in Table 2, there are substantial differences in the volume transports of the two AW branches from occupation to occupation. There is also variability in the temperature of the two cores. For each occupation we tabulated the mean temperature of each branch. This revealed that the onshore branch varies more in temperature than the offshore branch; the range of the former is 0.14°C compared to 0.09°C for the latter. There is no clear relationship between the two, nor is there a significant correlation between the temperature and volume transport of each branch. The lack of correlation with the transport is not particularly surprising since temperature acts more like a tracer that is less sensitive to mesoscale variability than velocity. It is perhaps more puzzling that the two temperature cores do not covary, since the two branches originate from a single current entering the Canadian Basin (Woodgate et al., 2007). However, as shown below, the upstream pathways of the two branches differ markedly. The onshore branch is likely subject to stronger and more variable mixing, which could lead to temperature variations that are not present in the offshore branch. Furthermore, the different path lengths of the two branches result in different propagation times of temperature anomalies emanating from upstream, also causing out of sync variability. This is addressed in section 5.2 below.

It still remains to be determined what dictates the transport variability in Table 2. One obvious possibility is wind forcing. Pickart et al. (2011) demonstrated that the rebound jet of AW spins up at the tail end of an upwelling event driven by easterly winds. A signature of the rebound jet was present in four of the DBO6 occupations, with a range in transport of 0.18 to 1.67 Sv. In each case there were easterly winds preceding the occupation of the section. We computed the alongcoast winds during and prior to the occupation of the eight sections that had transport estimates of the onshore and offshore AW branches. No consistent relationship was found between the wind speed and the volume flux for either branch.

Since the Beaufort Gyre is situated above the two branches of AW, this motivated us to consider wind stress curl forcing as well. The idea is that, since the gyre strength is largely dictated by the wind stress curl over the Canada Basin (Dosser & Timmermans, 2018), this might influence the eastward flow beneath the gyre. For each occupation we averaged the wind stress curl over the region denoted in Figure 1b, for the 30 day period prior to the occupation (results were not sensitive to the exact length of time chosen for the average) and compared it to the corresponding transport of each branch, as well as the total transport (Figure 6). For both the onshore and offshore branches and the combined flow, there appears to be a connection between the wind stress curl and the volume transport in that the more negative the wind stress curl, the weaker the flow of AW. While this is not statistically significant due to the small number of DBO6 realizations, it is confirmed for the onshore branch using the velocity time series from the offshoremost mooring of the SBI array (Figure 2b). The weakened eastward flow of the AW is presumably associated with a stronger westward flow of the Beaufort Gyre in the upper layer, and vice versa; however, we cannot test this with our data because, as noted above in Figure 4a, the DBO6 section did not extend far enough offshore to capture the full extent of the gyre.

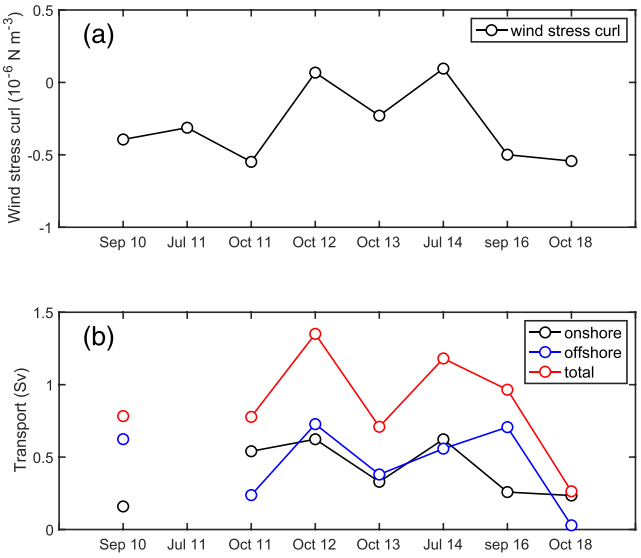

Figure 6. (a) Wind stress curl (10^{-6} N m^{-3}) in the Canada Basin, and (b) volume transport (Sv) of onshore branch (black), offshore branch (blue), and both branches combined (red). See text for details. There were no values of volume transport for the 2003 occupation and the July 2011 occupation.

4. *T/S* Structures

Previous studies have used characteristic signatures in *T/S* space to investigate the dynamics, time history, and pathways of the AW in the Canadian Basin (McLaughlin et al., 2009; Woodgate et al., 2007). This motivates us to consider the DBO6 transect data from this perspective to see if it sheds light on the nature of the boundary current system here. Using a hydrographic data set from the Chukchi Borderland region, Woodgate et al. (2007) identified five classes of *T/S* signatures that resulted from different mixing mechanisms involving time-varying AW and adjacent waters. They used this information to construct a circulation scheme of the FSBW and BSBW flowing across the Mendeleev Ridge through the Chukchi Borderland. Subsequent to this, McLaughlin et al. (2009) used the same methodology to investigate the circulation and spreading of FSBW into the Canada Basin, including the role of the Beaufort Gyre.

Of relevance to our study are the *T/S* signatures referred to by Woodgate et al. (2007) as "zigzag," "point and bump," and "smooth." Examples of these are shown in Figure 7 from our DBO6 data. The zigzag shape (Figure 7a, orange curve) results from double-diffusive mixing of different water types (Woodgate et al., 2007), which is commonly observed throughout the Arctic Ocean. The more disparate the two parent water masses, the more pronounced the resulting zigzag. Woodgate et al. (2007) differentiated between large and small zigzags; they also considered a separate class referred to as ragged zigzags, which were not present in our data set. The point and bump shape (Figure 7a, red curve) arises when double diffusion is not as prevalent and turbulent mixing has a significant influence. The smooth *T/S* class (Figure 7b, blue curve) occurs when mechanical mixing is strong enough to erase all double-diffusive signatures. We identified an additional *T/S* signature in our data set that was not discussed by Woodgate et al. (2007) in the Chukchi Borderland region or McLaughlin et al. (2009) in the Canada Basin. This is shown by the black curve in Figure 7c, which we refer to as a "chaotic" signature.

In this study, we consider three *T/S* classes: point and bump/large zigzag (Type 1); smooth (Type 2); and chaotic (Type 3), which together account for the vast majority of the profiles. As noted above, we did not observe any ragged zigzag profiles. Figure 7 shows the division of all of the DBO6 profiles into these three categories (the gray lines in each of the panels). We note that there were only a few profiles with large zigzags in our data set (one of them is highlighted orange in Figure 7a). While there were a fair number of cases that could be classified as very small zigzags, in our analysis we smoothed all of the *T/S* profiles using a 15-point

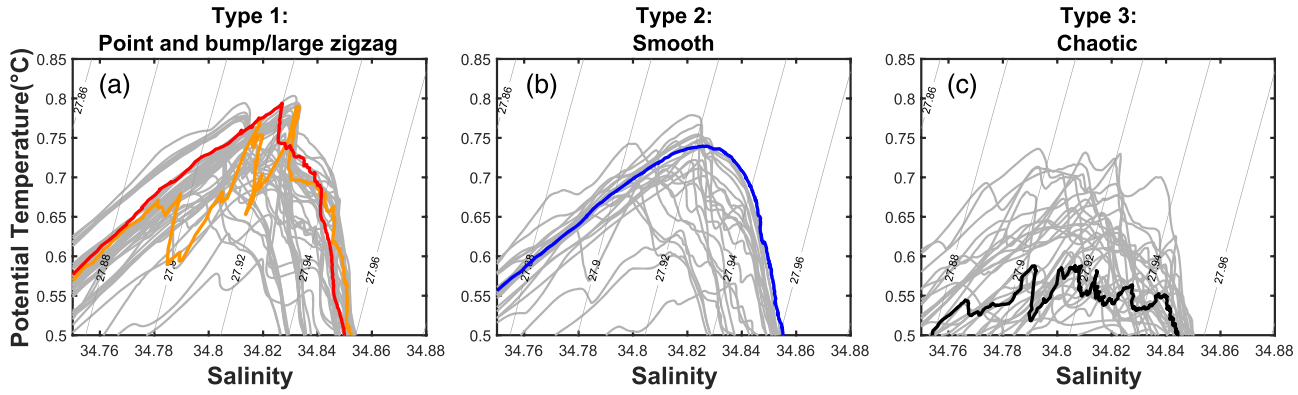

Figure 7. Groupings of stations in the DBO6 data set into the three *T/S* types considered in the study. The thick gray lines are the individual profiles. A representative example of each type is highlighted in color:point and bump (red); large zigzag (orange); smooth (blue); and chaotic (black). The light gray contours are potential density (kg m^{-3}).

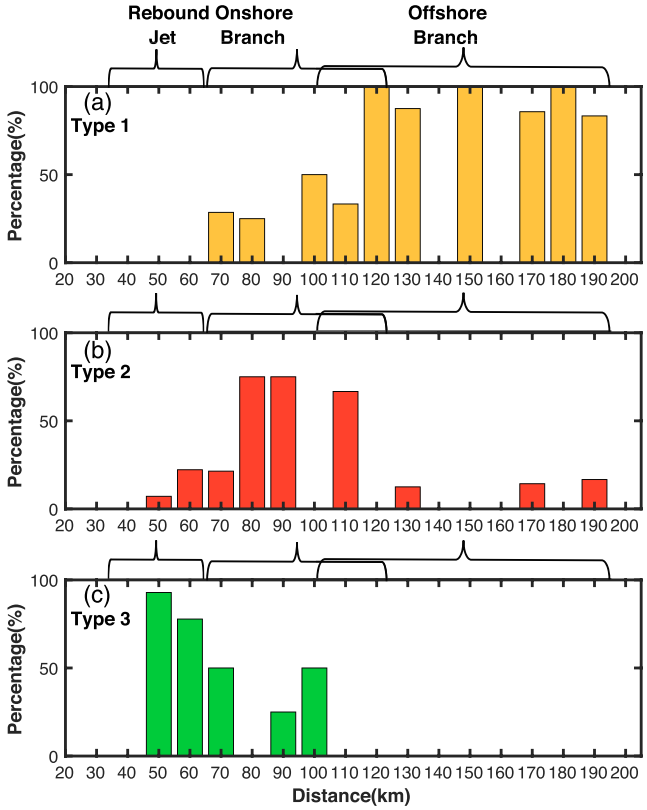

Figure 8. Geographical distribution along the DBO6 line of the three *T*/*S* types shown in Figure 7. The *y* axis is the percentage of each type at each cross-stream grid point. The range in locations of the three components of the AW boundary current are marked.

filter, which removed these signatures (i.e., made them indistinguishable from the smooth profiles). For the purposes of our story, it was not necessary to consider a separate small zigzag class.

The Type 1 profiles are warmest and, for the DBO6 data, have a consistent signature of the point (the maximum temperature) and subsequent bump (immediately below this in the water column, to the right in the *T*/*S* diagram). The Type 2 profiles are also tightly grouped, but generally not as warm. By contrast, the Type 3 profiles display much more variability in *T*/*S* space and have the lowest temperature. We note that some of the temperature variation within each grouping is due to the propagation of warm pulses on interannual time scales, as discussed in section 1; keep in mind the DBO6 data set spans 13 years. This is addressed below in section 5.2.

The three types of *T*/*S* classes have a clear geographical pattern along the DBO6 transect: Type 1 profiles are found predominantly offshore, Type 2 profiles are most common inshore of this, and Type 3 profiles are prevalently close to the continental slope. This is shown in Figure 8, which documents the percent occurrence of each *T*/*S* type as a function of cross-stream distance. Marked on the figure is the range in locations of the two AW branches, as well as the rebound jet. One sees that each component of the boundary current system is dominated by a different *T*/*S* type. The offshore branch is mostly characterized by Type 1, the onshore branch is predominantly Type 2, and the rebound jet region is mostly Type 3.

Woodgate et al. (2007) found that the point and bump structure dominated in the core of the AW boundary current in the Chukchi Borderland region, noting that the enhanced velocity and mixing in the current would tend to erode the double-diffusive structure. This is consistent with the observations of McLaughlin et al. (2009) in the vicinity of the Northwind Ridge. By contrast, Woodgate et al.'s (2007) observations of smooth *T*/*S* structures were limited to stations close to the Chukchi continental slope, where they argued that stronger mechanical mixing would tend to cause this. This is in line with the McLaughlin et al. (2009) measurements near the Beaufort continental slope, which showed the presence of small zigzags and smooth profiles.

These previous observations are consistent with our results, in that the onshore AW branch is closer to the continental slope, hence smooth profiles would tend to dominate there, while point and bump profiles would dominate in the offshore branch. This is elaborated on in section 5.1 where we investigate the upstream paths of the two branches. Finally, as noted above, Woodgate et al. (2007) did not observe chaotic profiles in their data set. This is likely because they did not sample near the shelfbreak, where particularly energetic processes such as upwelling, downwelling, and the rebound jet lead to intense mixing of cold Pacific winter water and warm Atlantic water (Lin et al., 2019). We surmise that this strong mixing leads to the chaotic *T*/*S* profiles in the vicinity of the shelfbreak. The absence of chaotic profiles in the McLaughlin et al. (2009) data set is likely due to their coarse station spacing near the boundary.

5. Pathways of the Atlantic Water Boundary Current

As discussed above, previous studies have investigated the flow of AW as it progresses across the Mendeleev Ridge, through the Chukchi Borderland, and into the Canada Basin. The detailed topography of the region is shown in Figure 9a. The Chukchi Borderland, which is located east of the Mendeleev Ridge, is comprised of the following bathymetric features (progressing west to east): the Chukchi Abyssal Plain; the Chukchi Rise (also known as the Chukchi Plateau or Chukchi Cap); the Northwind Abyssal Plain; and the Northwind Ridge (the eastern side of the Northwind Ridge descends very steeply into the Canada Basin). Another important feature is the Chukchi Gap, the ~1,000 m deep channel through the Chukchi Rise (Figure 9a).

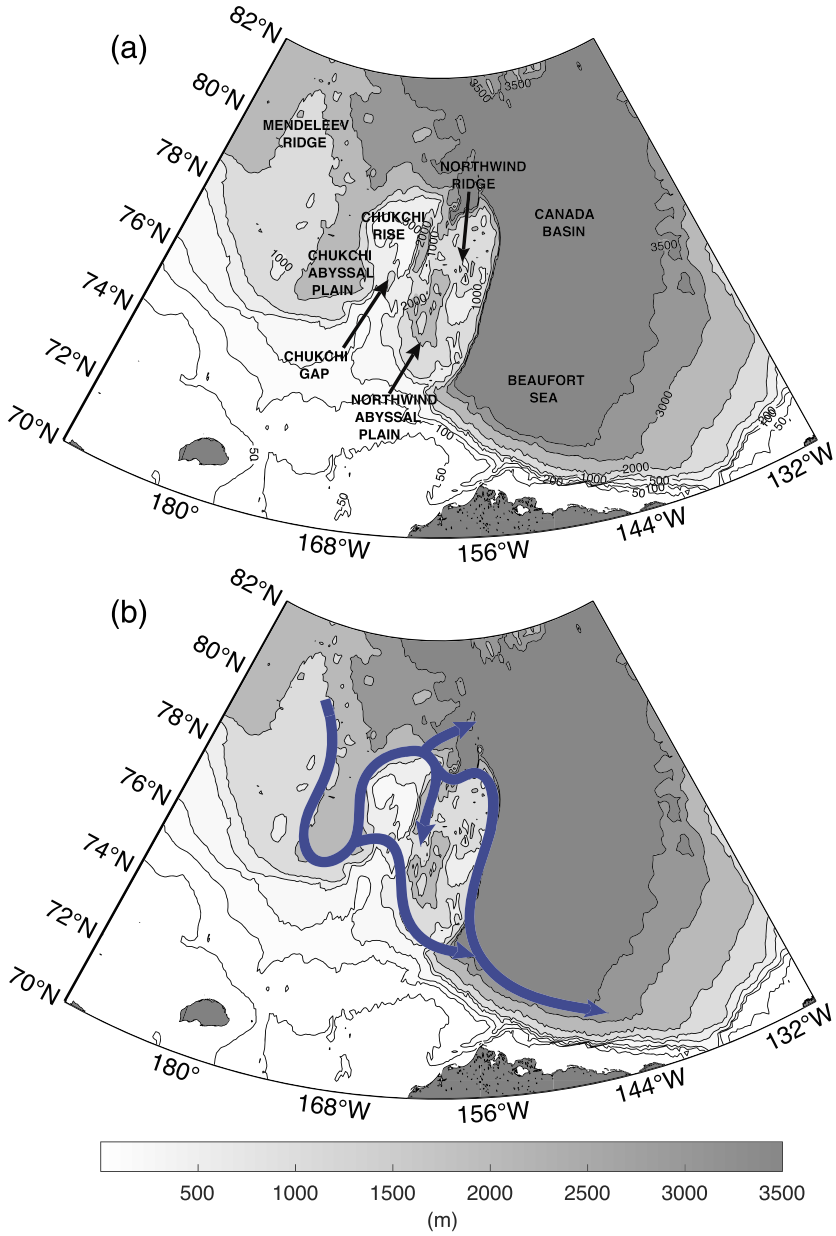

Figure 9. (a) Detailed bathymetry of the study area and place names identifying the different parts of the Chukchi Borderland. (b) Schematic flow lines of the AW boundary current based on previous studies (see text for details).

Figure 9b summarizes the findings of Shimada et al. (2004), McLaughlin et al. (2004), Woodgate et al. (2007), and McLaughlin et al. (2009), all of whom deduced different aspects of the AW pathways in this region based on a combination of temperature propagation, *T/S* structures, velocity information, and assumptions about flow along *f/H* contours (where *f* is the Coriolis parameter and *H* is the bottom depth). The basic flow pattern that emerges from these studies is as follows (Figure 9b). The AW approaches the Chukchi Rise as a single current that subsequently bifurcates. Some of it progresses eastward through the Chukchi Gap, which is considered the continental slope branch (both Shimada et al., 2004, and McLaughlin et al., 2004, noted this branch, although Woodgate et al., 2007, did not see evidence of it in their data). The remainder of the AW flows northward then eastward around the top of the Chukchi Rise. At this point the flow divides further: Some portion continues around the top of the Northwind Ridge, some of it turns southward and progresses along the eastern side of the Chukchi Rise, and a fraction is diverted into the Canada Basin. This latter

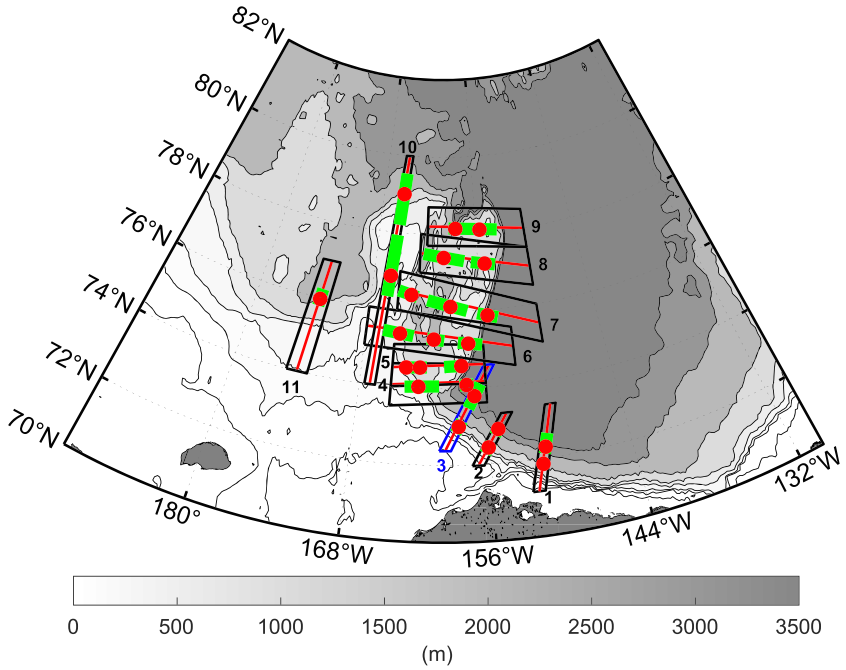

Figure 10. Locations of the sections (numbered 1–11 downstream to upstream) constructed using the UDASH data and the corresponding temperature cores. The data points within each rectangle were projected onto the red line in the middle of the rectangle to create the section. The green segments show the extent of each warm water core, and the red circles mark the center of the core (see Figure 11). The blue rectangle denotes Section 3, which is shown in Figure 11.

pathway is supported by tracer measurements (Smith et al., 1999), and McLaughlin et al. (2009) argue that the separated flow gets entrained into the anticyclonic Beaufort Gyre. Finally, the flow on the north side of the Northwind Ridge turns southward along the east side of the ridge and eventually combines with the continental slope branch as a single current that flows into the Beaufort Sea.

Our repeat DBO6 transects have revealed that the AW boundary current—seaward of the rebound jet—is in fact composed of two branches in the Alaskan Beaufort Sea. We now investigate the reason for this using the UDASH historical data and, in so doing, put our results in context with the previous studies.

5.1. Pathways Through the Chukchi Borderland and Chukchi Slope

The UDASH data coverage seaward of the 200 m isobath is shown in Figure 1b. The approach we took to infer the AW pathways was to construct vertical sections across the major bathymetric features, with the easternmost section corresponding to the DBO6 line, and the westernmost section situated upstream of the Chukchi Rise (Figure 10). This approach was more interpretable than making lateral maps (where, among other things, it was hard to choose an appropriate grid spacing). Each section used data within a swath (the black/blue rectangles in the figure), where the stations were projected onto a single line centered within the swath (the red lines in the figure) and the data subsequently gridded using Laplacian-Spline interpolation with a horizontal grid spacing of 20 km and a vertical grid spacing of 20 m. Some swaths are wider than others and there is some partial overlap; this was dictated by the uneven data coverage. Encouragingly, the vertical section constructed along the DBO6 line—excluding our occupations—showed the inshore and offshore temperature cores.

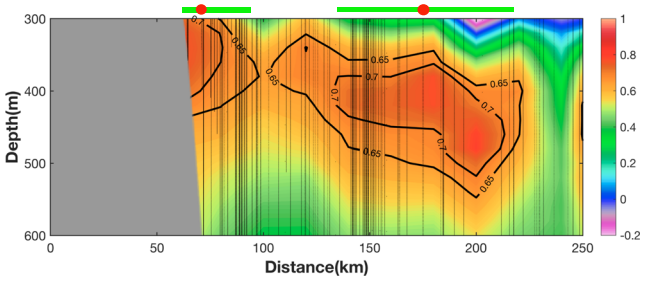

Figure 11. Composite vertical section of potential temperature for Section 3, marked by the blue rectangle in Figure 10. The vertical lines show the CTD casts used for the composite. The green segments above the plot denote the extent of the two temperature cores, and the red circles denote the center of the cores.

The temperature section corresponding to the transect across the Chukchi slope in Figure 10 denoted by the blue rectangle is shown in Figure 11. This reveals the presence of two temperature cores in

Table 3
The Number of Type 1 Profiles (n) Versus the Total Number of Profiles (N) for Each Temperature Core Along the 11 Lines of Figure 10 (Numbered From Downstream to Upstream)

Lines/ Cores	1	2	3	4	5	6	7	8	9	10	11
a	4/ 17	0/ 7	4/ 17	10/ 31	6/7	3/10	4/9	10/ 10	3/3	0/ 2	4/ 6
b	11/ 14	2/ 2	5/ 5	19/ 20	8/10	12/14	10/10	2/2	33/ 41	7/ 9	—
c	—	—	—	—	18/28	13/13	11/11	—	—	—	—

Note. The associated percentages are shown in Figure 12. The cores a, b, and c are ordered from south to north or from west to east for each line.

the FSBW layer, one adjacent to the continental slope and the other farther offshore in the basin. Consistent with our DBO6 occupations, the onshore temperature core is not as warm as that of the offshore core. In the figure, we have marked the cross-stream extent of the two cores (green lines) and the center of the two cores (red circles). This was done for each of the transects; that is, all of the cores were identified and their extent and center location documented in Figure 10.

In addition to using this evidence for deducing flow paths, we also considered the information provided by the *T/S* structures discussed above. However, instead of assessing the three different types of *T/S* profiles shown in Figure 7 throughout the domain, we took a simpler approach. In particular, we defined a box around the location of each temperature core in Figure 10 (i.e., encompassing the individual red circles), and computed the percentage P of Type 1 profiles within each box: $P = \frac{n}{N}$, where n is the number of Type 1 profiles and N is the total number of CTD stations within the box (Table 3). Importantly, we restricted the time interval for this calculation to the period when the warmest temperatures were present at each core location; in particular, as the largest temperature anomaly propagated through the domain (this propagation is addressed below in section 5.2). As noted in Woodgate et al. (2007), the *T/S* structures vary depending on the parent water masses, so it made for a cleaner analysis to consider only this warm phase, from 2000 to 2007. The resulting values of P are shown in Figure 12 for this time period, which range from near-zero to almost 100%.

Using the distribution of temperature cores together with the Type 1 percentages (Figures 10 and 12), we traced out the likely pathways of the AW (Figure 13). Not surprisingly, our circulation scheme is similar to the composite pattern deduced by earlier studies. There are, however, important differences. One difference concerns the flow branch extending southward from the northeast part of the Chukchi Rise. The earlier analyses suggested that this branch flows along the eastern side of the rise (i.e., west of the Northwind Abyssal Plain) with an unsure fate. Our evidence implies that this branch progresses along the western side of the Northwind Ridge (i.e., east of the Northwind Abyssal Plain) and joins the Chukchi continental slope branch of AW. This is suggested by both the temperature core distribution and the P distribution; that is, there are high percentages of Type 1 all along this branch.

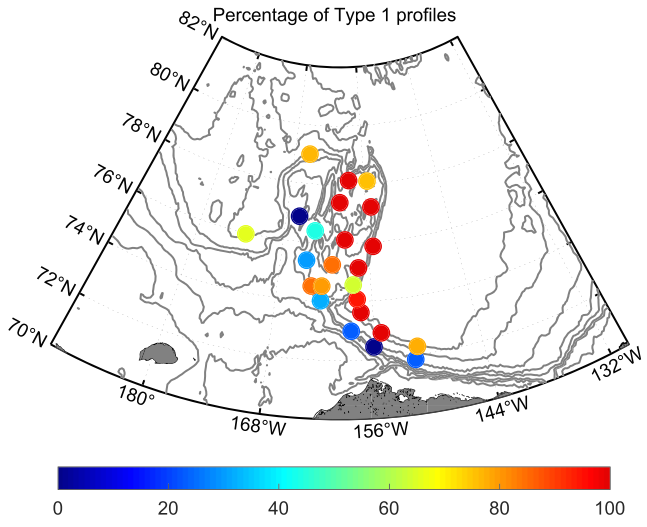

Figure 12. Percentage of Type 1 profiles in the region surrounding each of the temperature cores of Figure 10. The contoured isobaths are 40, 50, 100, 200, 500, 1,000, 2,000, 3,000, and 3,500 m.

Consistent with the earlier studies, we see only a single AW flow branch stemming from the Mendeleev Ridge, with a relatively large value of P (near 70%). Interestingly, this percentage drops to small values for the part of the current that diverts through the Chukchi Gap (Figure 12), which suggests enhanced mixing takes place as the water negotiates this complex bathymetric feature. The value of P in the continental slope branch remains small (<35%) as the flow progresses eastward, except for two locations. The first is where the branch west of the Northwind Ridge merges with it, as noted above. The second is just beyond the Chukchi Gap, which leads us to draw an additional minor flow branch to the west of the Northwind Abyssal Plain that merges with the slope branch.

The most notable difference between the earlier circulation pattern (Figure 9b) and that presented here (Figure 13) is that, in our scheme, two branches of AW emerge from the Chukchi Borderland. This is indicated by the presence of two temperature cores on all three sections east of the Borderland. Furthermore, there is a distinct difference in the Type 1 percentages in the two branches. The conclusion is that the inner branch seen in our DBO6 sections is the downstream extension of the slope branch that passed through the Chukchi Gap, with a contribution from the outer Borderland branch that bifurcated

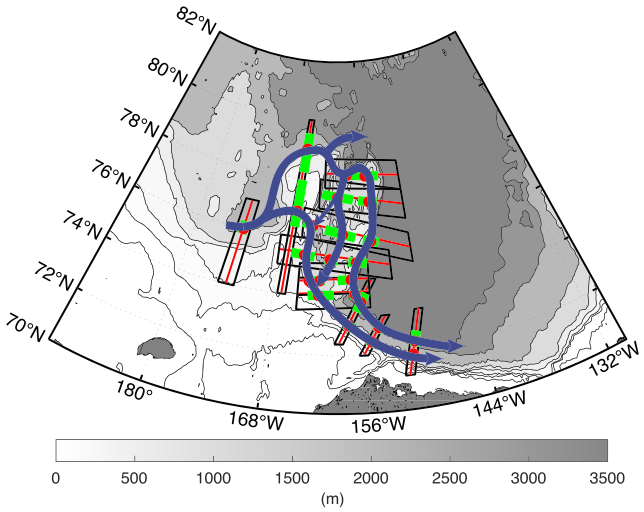

Figure 13. Circulation scheme of the FSBW (blue arrows) based on the temperature cores and percentages of Type 1 *T/S* profiles (see text for details).

as that flow encountered the Northwind Ridge. In contrast, the offshore branch seen in our DBO6 line is a continuation of the portion of the outer Borderland pathway that flowed along the east side of the Northwind Ridge. Furthermore, the evidence suggests that the inner branch at the DBO6 line, stemming from the Chukchi Gap, is consistently subject to stronger mechanical mixing. The composite scheme presented here implies that the two branches in the Canada Basin should have different histories in terms of the propagation of warm temperature anomalies from upstream. We investigate this next.

5.2. Interannual AW Core Potential Temperature Variation

As mentioned in section 1, warm pulses of AW emanating from Fram Strait are known to propagate cyclonically around the Arctic Ocean in the AW boundary current on interannual time scales, cooling as they do so (e.g., Dmitrenko et al., 2008; Polyakov et al., 2005, 2011). The first documented pulse in Fram Strait occurred around 1990, and a second pulse was identified roughly 10 years later. The second pulse was warmer than the first. Using a combination of mooring records and shipboard hydrographic measurements, propagation times of the two pulses have been estimated. Shimada et al. (2004) tracked the arrival of the first pulse in the Canada Basin and through the Chukchi Borderland; that is, through both the northern and southern pathways noted above. Inspection of the lateral temperature maps in Shimada et al. (2004) indicates that the leading edge of the first pulse reached the Borderland 4–6 years after entering Fram Strait.

The pathway and timing of the second, warmer pulse that entered Fram Strait around 2000 has been investigated by various authors. Polyakov et al. (2005) tracked the pulse from Fram Strait to the northern Laptev Sea, indicating a propagation time of 4 years. Dmitrenko et al. (2008) traced the pulse along the Lomonosov Ridge (in the bifurcated branch of the AW boundary current), calculating a faster propagation speed than farther upstream. Interestingly, the data presented by Dmitrenko et al. (2008) imply that the second pulse spread more effectively along the Lomonosov branch of the current than in the continental slope branch. Polyakov et al. (2011) showed that it took two more years for the warm water to arrive on the east side of the ridge. This suggests that the second warm pulse took longer to reach the western Arctic than the first pulse, perhaps due to variability in the bifurcation process. Presently, the second warm pulse has not been conclusively detected or tracked in the Canadian Basin, although Polyakov et al. (2011) reported anomalously warm AW temperatures in 2009 on the northern side of the Northwind Ridge.

In light of the above studies, one might expect a travel time of ~4 years for a warm water pulse to reach the Lomonosov Ridge, and perhaps another 2–4 years for the water to reach the southwestern part of the Chukchi Borderland. Again, note that this is for the leading edge of the pulse.

Using the UDASH data, we endeavored to document the propagation of warm anomalies through the Chukchi Borderland into the Canada Basin. Note that this is impossible to do using the set of sections defined in Figure 10 due to the sparseness of the UDASH data, since the aim here is to construct time series with yearly resolution. Therefore, we defined three fairly broad regions: an upstream region immediately to the west of the Chukchi Rise, which documents the temperature of the AW encroaching the Borderland; a northern region which characterizes the outer branch of the flow around the Borderland; and a downstream region in the southern Canada Basin. While we are unable to document the two branches separately in the downstream region with yearly resolution, it is still instructive to consider their composite signal.

For each region, we constructed a yearly time series of temperature averaged within the core of the FSBW, where the core was taken to be the density layer 27.90–27.94 kg m^{-3} (recall that the full FSBW density layer is 27.06–27.97 kg m^{-3}, see Figure 3a). The result is shown in Figure 14, where the standard errors are included. In years where there were very little data in a given region (less than five profiles), no value is reported. In the upstream region, the temperature warms rapidly in the 1990s, reaching its maximum value around 1998. This is clearly the arrival of the first warm pulse, which is consistent with the studies noted

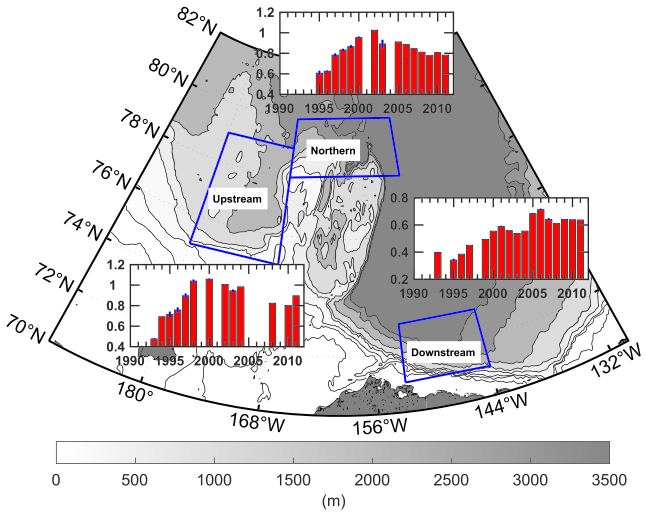

Figure 14. Interannual variation of the FSBW core potential temperature (°C), averaged over the density layer 27.90–27.94 kg m^{-3}, in the three regions denoted by the blue boxes. The standard errors are included. In years when there were less than five profiles, no value is reported.

above. After decreasing through the first decade of the 2000s there is evidence of another warming trend in this region starting around 2010, which we interpret as the arrival of the second warm pulse.

Considering the northern region next, the temperature peaks around 2002, roughly 4 years after the peak in the upstream region. This is consistent with the conclusions of Woodgate et al. (2007) regarding the outer AW branch that advects the warm, high *P* water around the seaward edge of the Borderland. Such a time lag implies an advective speed of ~0.6 cm s^{-1}, which is in line with the measured value of 0.8 cm s^{-1} for the offshore branch at the DBO6 line which is fed by the outer Borderland branch.

Finally, the time series for the downstream region shows an initial temperature peak around 2001, followed by a second peak occurring around 2006. It seems likely that these two peaks represent the different pathways by which the AW proceeds from the Borderland to the Canada Basin—in particular, the slope branch versus the outer branch (realizing that there is communication between these two routes via the branch flowing southward along the western side of the Northwind Ridge, Figure 13). Again, the implied advective speeds are reasonable. The 3 year lag for the slope branch (1998 to 2001) implies a speed of 1.1 cm s^{-1}, versus the measured value of 1.2 cm s^{-1} for the onshore branch at the DBO6 line (which is fed by the slope branch). For the outer branch progressing from the top of the Borderland along the eastern side of the Northwind Ridge, the 4 year lag (2002–2006) gives a speed of 0.9 cm s^{-1} compared to the measured value of 0.8 cm s^{-1} for offshore branch at the DBO6 line. The smaller maximum temperature in the downstream region is likely a reflection of the enhanced mixing along the slope route. Overall, the progression of the 1990 Fram Strait AW warm pulse through our study area, documented in Figure 14, agrees well with the circulation scheme deduced from the historical hydrography together with the DBO6 measurements.

6. Conclusions

In this study, we have used a combination of synoptic shipboard measurements, historical hydrographic data, and satellite data to advance our understanding of the AW boundary current as it progresses from the Chukchi Borderland into the Canada Basin. A set of nine repeat, high-resolution occupations of the DBO6 line in the Alaskan Beaufort Sea, taken between 2003 and 2018, revealed that the current is composed of two main branches. These reside seaward of the narrow, intermittent rebound jet of AW, and flow beneath/counter to the Beaufort Gyre. The onshore branch, located in the bottom depth range of 1,000–1,500 m, transports 0.40 ± 0.07 Sv, while the offshore branch, in the bottom depth range of 2,500–3,000 m, transports 0.47 ± 0.10 Sv. Each branch corresponds to a distinct temperature core. The year-to-year variability in transport of the individual branches, as well as the total transport, appears to be related to the wind stress curl in the Canada Basin, which drives the Beaufort Gyre. However, this needs to be further quantified with additional data.

The three components of the AW boundary current system are associated with unique *T/S* signatures. The offshore branch is mainly characterized by a point and bump shape, indicative of some degree of mixing that erodes the double-diffusive signature that would otherwise be present (consistent with the results of Woodgate et al., 2007). The onshore branch is instead dominated by a smooth *T/S* shape, which implies even stronger mechanical mixing as this branch is closer to the continental slope. By contrast, the energetic upper slope consists mainly of chaotic *T/S* shapes, presumably due to the mixing of warm and cold waters.

To investigate why there are two branches of AW water in the Canada Basin versus a single branch, we used the UDASH historical database to trace the warm water upstream. In particular, we constructed composite vertical sections of temperature at strategically placed transects extending westward from the DBO6 line through the Chukchi Borderland. This revealed distinct temperature cores along each of the transects,

from which warm water pathways could be deduced. Examining the *T/S* structures of the stations comprising these cores added further confirmation of these pathways.

The resulting circulation scheme is consistent with the composite scheme based on a number of previous studies, with important differences. Most notably, the onshore branch in the Canada Basin is shown to be the downstream extension of the continental slope branch that flows through the Chukchi Gap, with a contribution from an interior branch through the Borderland. In contrast, the offshore branch in the Canada Basin is the continuation of the outer Borderland branch that stems from the eastern side of the Northwind Ridge. As such, the single AW current that enters the Borderland from the Mendeleev Ridge undergoes a series of bifurcations that ultimately results in two branches flowing into the Canada Basin.

Lastly, it was shown that this flow scheme is consistent with the propagation of warm temperature anomalies originating from Fram Strait as they encounter the Chukchi Borderland and emanate into the Canada Basin. The warm pulse stemming from Fram Strait in 1990 reached the region immediately upstream of the Borderland in 1998, after which the temperature decreased again through the first decade of the 2000s. The subsequent increase starting in 2010 may be the signature of the second warm pulse that originated from Fram Strait in 2000. The region of the northern Borderland showed a peak temperature in 2002, consistent with the estimated advective speed of the outer AW branch. In the downstream region of the Canada Basin there were two temperature peaks separated by 5 years, consistent with the difference in advective speeds and distances of the continental slope branch and outer Borderland branch.

While this study has sharpened our view of the AW boundary current system in the Canadian Arctic, further aspects of the circulation remain to be explored. As mentioned above, while our data suggest that the two main AW branches in the Canada Basin vary in response to the regional wind stress curl, this needs to be verified with a longer time series. In addition, the fate of the AW branch that separates from the top of the Borderland needs to be investigated. McLaughlin et al. (2009) argued that this warm water circulates anticyclonically with the Beaufort Gyre, opposite to the two AW branches identified here. This in turn raises questions about possible storage of warm water in the Canada Basin. The overall relationship between the flow of AW and the Beaufort Gyre needs to be explored both from a kinematic and dynamical perspective. Finally, there is the question of the fate of the warm AW as it continues farther eastward toward the Canadian Arctic Archipelago and ultimately Fram Strait, from whence it originated.

Data Availability Statement

The DBO6 shipboard hydrographic and velocity data can be found at this site (http://aon.whoi.edu/).

Acknowledgments

The authors are indebted to the many officers and crew members of the USCGC *Healy*, R/V *Nathan B. Palmer*, and R/V *Sikuliaq* who helped collect the data on the DBO6 transects, and to the many individuals who processed the hydrographic data. We acknowledge J. Swift, who was chief scientist on the first occupation. This work was funded by the following sources: National Science Foundation Grants PLR-1504333, OPP-1733564, and OPP-1504394; National Oceanic and Atmospheric Administration Grant NA14OAR4320158; and National Aeronautics and Space Administration Grant NNX10AF42G.

References

Aksenov, Y., Ivanov, V. V., Nurser, A. G., Bacon, S., Polyakov, I. V., Coward, A. C., et al. (2011). The Arctic circumpolar boundary current. *Journal of Geophysical Research*, *116*, C09017. https://doi.org/10.1029/2010JC006637

Armitage, T. W., Bacon, S., Ridout, A. L., Thomas, S. F., Aksenov, Y., & Wingham, D. J. (2016). Arctic sea surface height variability and change from satellite radar altimetry and GRACE, 2003–2014. *Journal of Geophysical Research: Oceans*, *121*, 4303–4322. https://doi.org/10.1002/2015JC011579

Behrendt, A., Sumata, H., Rabe, B., & Schauer, U. (2018). UDASH–Unified database for Arctic and subarctic hydrography. *Earth System Science Data*, *10*(2), 1119–1138. https://doi.org/10.5194/essd-10-1119-2018

Brugler, E. T., Pickart, R. S., Moore, G. W. K., Roberts, S., Weingartner, T. J., & Statscewich, H. (2014). Seasonal to interannual variability of the Pacific water boundary current in the Beaufort Sea. *Progress in Oceanography*, *127*, 1–20. https://doi.org/10.1016/j.pocean.2014.05.002

Cokelet, E. D., Tervalon, N., & Bellingham, J. G. (2008). Hydrography of the West Spitsbergen current, Svalbard Branch: Autumn 2001. *Journal of Geophysical Research*, *113*, C01006. https://doi.org/10.1029/2007JC004150

Dmitrenko, I. A., Polyakov, I. V., Kirillov, S. A., Timokhov, L. A., Frolov, I. E., Sokolov, V. T., et al. (2008). Toward a warmer Arctic Ocean: Spreading of the early 21st century Atlantic water warm anomaly along the Eurasian Basin margins. *Journal of Geophysical Research*, *113*, C05023. https://doi.org/10.1029/2007JC004158

Dosser, H. V., & Timmermans, M.-L. (2018). Inferring circulation and lateral eddy fluxes in the Arctic Ocean's deep Canada Basin using an inverse method. *Journal of Physical Oceanography*, *48*(2), 245–260. https://doi.org/10.1175/JPO-D-17-0190.1

Koenig, Z., Provost, C., Sennéchael, N., Garric, G., & Gascard, J. C. (2017). The Yermak Pass branch: A major pathway for the Atlantic water north of Svalbard. *Journal of Geophysical Research: Oceans*, *122*, 9332–9349. https://doi.org/10.1002/2017JC013271

Kolås, E., & Fer, I. (2018). Hydrography, transport and mixing of the West Spitsbergen current: The Svalbard Branch in summer 2015. *Ocean Science*, *14*, 1603–1618. ocean-sci-discuss.net. https://doi.org/10.5194/os-14-1603-2018

Ladd, C., Mordy, C. W., Salo, S. A., & Stabeno, P. J. (2016). Winter water properties and the Chukchi polynya. *Journal of Geophysical Research: Oceans*, *121*, 5516–5534. https://doi.org/10.1002/2016JC011918

Lin, P., Pickart, R. S., Moore, G., Spall, M. A., & Hu, J. (2019). Characteristics and dynamics of wind-driven upwelling in the Alaskan Beaufort Sea based on six years of mooring data. *Deep Sea Research Part II: Topical Studies in Oceanography*, *162*, 79–92. https://doi.org/10.1016/j.dsr2.2018.01.002

Lin, P., Pickart, R. S., Stafford, K. M., Moore, G., Torres, D. J., Bahr, F., & Hu, J. (2016). Seasonal variation of the Beaufort shelfbreak jet and its relationship to Arctic cetacean occurrence. *Journal of Geophysical Research: Oceans*, *121*, 8434–8454. https://doi.org/10.1002/2016JC011890

Lique, C., & Steele, M. (2012). Where can we find a seasonal cycle of the Atlantic water temperature within the Arctic Basin? *Journal of Geophysical Research*, *117*, C03026. https://doi.org/10.1029/2011JC007612

Mayer-Gürr, T., Savcenko, R., Bosch, W., Daras, I., Flechtner, F., & Dahle, C. (2012). Ocean tides from satellite altimetry and GRACE. *Journal of Geodynamics*, *59*, 28–38.

McLaughlin, F., Carmack, E., Macdonald, R., Melling, H., Swift, J., Wheeler, P., et al. (2004). The joint roles of Pacific and Atlantic-origin waters in the Canada Basin, 1997–1998. *Deep Sea Research Part I: Oceanographic Research Papers*, *51*(1), 107–128. https://doi.org/10.1016/j.dsr.2003.09.010

McLaughlin, F. A., Carmack, E. C., Macdonald, R. W., & Bishop, J. K. (1996). Physical and geochemical properties across the Atlantic/Pacific water mass front in the southern Canadian Basin. *Journal of Geophysical Research*, *101*(C1), 1183–1197. https://doi.org/10.1029/95JC02634

McLaughlin, F. A., Carmack, E. C., Williams, W. J., Zimmermann, S., Shimada, K., & Itoh, M. (2009). Joint effects of boundary currents and thermohaline intrusions on the warming of Atlantic water in the Canada Basin, 1993–2007. *Journal of Geophysical Research*, *114*, C00A12. https://doi.org/10.1029/2008JC005001

Meyer, A., Sundfjord, A., Fer, I., Provost, C., Villacieros Robineau, N., Koenig, Z., et al. (2017). Winter to summer oceanographic observations in the Arctic Ocean north of Svalbard. *Journal of Geophysical Research: Oceans*, *122*, 6218–6237. https://doi.org/10.1002/2016JC012391

Moore, S. E., Grebmeier, J. M., & Giguère, N. (2018). The distributed biological observatory. *Arctic*, *71*, 1–7.

Nansen, F. (1902). The oceanography of the North Polar Basin. The Norwegian North Polar Expedition 1893-1896. *Scientific Results*, *3*(9).

Newton, J. L., & Coachman, L. K. (1974). Atlantic Water circulation in the Canada Basin. *Arctic*, *27*, 297–303.

Nikolopoulos, A., Pickart, R. S., Fratantoni, P. S., Shimada, K., Torres, D. J., & Jones, E. P. (2009). The western Arctic boundary current at 152 W: Structure, variability, and transport. *Deep Sea Research Part II: Topical Studies in Oceanography*, *56*(17), 1164–1181. https://doi.org/10.1016/j.dsr2.2008.10.014

Padman, L., & Erofeeva, S. (2004). A barotropic inverse tidal model for the Arctic Ocean. *Geophysical Research Letters*, *31*, L02303. https://doi.org/10.1029/2003GL019003

Pérez-Hernández, M. D., Pickart, R. S., Torres, D. J., Bahr, F., Sundfjord, A., Ingvaldsen, R., et al. (2019). Structure, transport, and seasonality of the Atlantic Water boundary current north of Svalbard: Results from a yearlong mooring array. *Journal of Geophysical Research: Oceans*, *124*, 1679–1698. https://doi.org/10.1029/2018JC014759

Pickart, R. S., Moore, G., Torres, D. J., Fratantoni, P. S., Goldsmith, R. A., & Yang, J. (2009). Upwelling on the continental slope of the Alaskan Beaufort Sea: Storms, ice, and oceanographic response. *Journal of Geophysical Research*, *114*, C00A13. https://doi.org/10.1029/2008JC005009

Pickart, R. S., Spall, M. A., & Mathis, J. T. (2013). Dynamics of upwelling in the Alaskan Beaufort Sea and associated shelf–basin fluxes. *Deep Sea Research Part I: Oceanographic Research Papers*, *76*, 35–51. https://doi.org/10.1016/j.dsr.2013.01.007

Pickart, R. S., Spall, M. A., Moore, G. W., Weingartner, T. J., Woodgate, R. A., Aagaard, K., & Shimada, K. (2011). Upwelling in the Alaskan Beaufort Sea: Atmospheric forcing and local versus non-local response. *Progress in Oceanography*, *88*(1–4), 78–100. https://doi.org/10.1016/j.pocean.2010.11.005

Pickart, R. S., Weingartner, T. J., Pratt, L. J., Zimmermann, S., & Torres, D. J. (2005). Flow of winter-transformed Pacific water into the western Arctic. *Deep Sea Research, Part II*, *52*, 3175–3198.

Pnyushkov, A. V., Polyakov, I. V., Rember, R., Ivanov, V. V., Alkire, M. B., Ashik, I. M., et al. (2018). Heat, salt, and volume transports in the eastern Eurasian Basin of the Arctic Ocean from 2 years of mooring observations. *Ocean Science*, *14*(6), 1349–1371. https://doi.org/10.5194/os-14-1349-2018

Polyakov, I., Alekseev, G., Timokhov, L., Bhatt, U., Colony, R., Simmons, H., et al. (2004). Variability of the intermediate Atlantic water of the Arctic Ocean over the last 100 years. *Journal of Climate*, *17*(23), 4485–4497. https://doi.org/10.1175/JCLI-3224.1

Polyakov, I., Beszczynska, A., Carmack, E. C., Dmitrenko, I. A., Fahrbach, E., Frolov, I. E., et al. (2005). One more step toward a warmer Arctic. *Geophysical Research Letters*, *32*(17), L17605. https://doi.org/10.1029/2005GL023740

Polyakov, I., Timokhov, L., Alexeev, V., Bacon, S., Dmitrenko, I., Fortier, L., et al. (2010). Arctic Ocean warming contributes to reduced polar ice cap. *Journal of Physical Oceanography*, *40*(12), 2743–2756. https://doi.org/10.1175/2010JPO4339.1

Polyakov, I. V., Alexeev, V. A., Ashik, I. M., Bacon, S., Beszczynska-Möller, A., Carmack, E. C., et al. (2011). Fate of early 2000s Arctic warm water pulse. *Bulletin of the American Meteorological Society*, *92*(5), 561–566. https://doi.org/10.1175/2010BAMS2921.1

Rudels, B. (2012). Arctic Ocean circulation and variability-advection and external forcing encounter constraints and local processes. *Ocean Science*, *8*(2), 261–286. https://doi.org/10.5194/os-8-261-2012

Rudels, B., Jones, E., Anderson, L., & Kattner, G. (1994). On the intermediate depth waters of the Arctic Ocean. In *The polar oceans and their role in shaping the global environment*, *AGU Geophysical Monograph* (Vol. 85, pp. 33–46).Washington, DC: AGU.

Schauer, U., Rudels, B., Jones, E. P., Anderson, L. G., Muench, R. D., Bjork, G., et al. (2002). Confluence and redistribution of Atlantic water in the Nansen, Amundsen and Makarov basins. *Annales de Geophysique*, *20*(2), 257–273. https://doi.org/10.5194/angeo-20-257-2002

Shimada, K., McLaughlin, F., Carmack, E., Proshutinsky, A., Nishino, S., & Itoh, M. (2004). Penetration of the 1990s warm temperature anomaly of Atlantic Water in the Canada Basin. *Geophysical Research Letters*, *31*, L20301. https://doi.org/10.1029/2004GL020860

Smith, J. N., Ellis, K. M., & Boyd, T. (1999). Circulation features in the Central Arctic Ocean revealed by nuclear fuel reprocessing tracers from scientific ice expeditions 1995 and 1996. *Journal of Geophysical Research*, *104*(C12), 29,663–29,677. https://doi.org/10.1029/1999JC900244

Spall, M. A., Pickart, R. S., Fratantoni, P. S., & Plueddemann, A. J. (2008). Western Arctic shelfbreak eddies: Formation and transport. *Journal of Physical Oceanography*, *38*(8), 1644–1668. https://doi.org/10.1175/2007JPO3829.1

Swift, J., Jones, E., Aagaard, K., Carmack, E., Hingston, M., Macdonald, R., et al. (1997). Waters of the Makarov and Canada basins. *Deep Sea Research Part II: Topical Studies in Oceanography*, *44*(8), 1503–1529. https://doi.org/10.1016/S0967-0645(97)00055-6

Woodgate, R. A., Aagaard, K., Muench, R. D., Gunn, J., Björk, G., Rudels, B., et al. (2001). The Arctic Ocean boundary current along the Eurasian slope and the adjacent Lomonosov Ridge: Water mass properties, transports and transformations from moored instruments. *Deep Sea Research Part I: Oceanographic Research Papers*, *48*(8), 1757–1792. https://doi.org/10.1016/S0967-0637(00)00091-1

Woodgate, R. A., Aagaard, K., Swift, J. H., Smethie, W. M. Jr., & Falkner, K. K. (2007). Atlantic Water circulation over the Mendeleev Ridge and Chukchi Borderland from thermohaline intrusions and water mass properties. *Journal of Geophysical Research*, *112*, C02005. https://doi.org/10.1029/2005JC003416